Chemical Engineering Journal 430 (2022) 133140

Contents lists available at ScienceDirect

Chemical Engineering Journal

journal homepage: www.elsevier.com/locate/cej

Energetic characteristics of hydrogenated amorphous silicon nanoparticles

Feiyu Xu [a,b], Giorgio Nava [a], Prithwish Biswas [a], Isabelle Dulalia [a], Haiyang Wang [a], Zaira Alibay [a], Mark Gale [a], Dylan J. Kline [a,b], Brandon Wagner [a], Lorenzo Mangolini [a,*], Michael R. Zachariah [a,*]

[a] University of California, Riverside, CA 92551, United States
[b] University of Maryland, College Park, MD 20742, United States

ARTICLE INFO

Keywords:
Silicon
Nanoparticles
Amorphous
Nanoenegetic
Combustion

ABSTRACT

In this work, we utilize a low-temperature non-equilibrium plasma to nucleate and grow sub-10 nm Si particles with varying degrees of crystallinity by tuning the level of power coupled into plasma discharge. Temperature-programmed desorption spectroscopy shows that as-prepared amorphous Si nanoparticles (*a*-nSi) incorporate more hydrogen than crystalline Si nanoparticles (*c*-nSi). Further, hydrogen is incorporated in the material in the form of higher silicon hydrides with a lower desorption temperature. Combustion cell measurements show that when formulated with $KClO_4$, *a*-nSi outperforms its crystalline counterpart with respect to pressure output. The pressurization rate of *a*-nSi/$KClO_4$ composite increases by a factor of six compared with nAl to 0.66 MPa·μs^{-1}. Evidence of hydrogen release (~730 K) from Temperature-jump time-of-flight mass spectrometry (T-Jump TOFMS) of *a*-nSi/$KClO_4$ suggests the creation of Si dangling bonds prior to ignition (~820 K), which then react exothermically with oxygen liberated from $KClO_4$, leading to ignition. Explosive reaction of H_2/O_2 mixture likely contributes to the rapid pressure rise. The enhanced energetic performance of hydrogenated *a*-nSi compared to its crystalline counterpart suggests that incorporation of hydrogen is a promising strategy for improving the performance of nanoenergetic materials.

1. Introduction

Silicon is a versatile material that has demonstrated promising applications in many areas, with nanoenergetics receiving some consideration [1–5]. Nanoenergetics, including nanothermites, are nanostructures that can undergo rapid and highly exothermic reactions. Si is thermodynamically a good candidate fuel with a gravimetric and volumetric energy density of 32.4 kJ·g^{-1} and 75.5 kJ·cm^{-3}, respectively, on par with Al (31.1 kJ·g^{-1} and 83.8 kJ·cm^{-3}), a benchmark for metal fuels [6]. Recent interest in Si-based nanoenergetic materials mainly lies in porous silicon (PS) films as a result of their extremely violent propagation and compatibility with on-chip integration [7–10]. Various oxidizers including perchlorates and nitrates have been used to impregnate the pores of PS to form energetic composites [11]. The flame propagation rate of PS-$NaClO_4$ composite was reported to be ~ 3050 m/s, exceeding the highest flame velocity of aluminum-based nanothermites by ~ 500 m/s [12]. The extraordinarily high combustion velocity of PS composites has been attributed to their enormous hydrogen-terminated surface (up to 910 m^2 g^{-1}) [12]. Research on the reactive properties of Si was further extended to free standing silicon nanoparticles, which prove to be significantly more reactive than micro-sized Si particles owing to reduced diffusion length scale and large surface area [13]. Crystalline Si nanotubes and nanowires were found to have reduced electrostatic discharge sensitivity, but their combustion velocity was also lower than aluminum-based nanothermites [14]. Through thermochemical calculations and experimental results, Mason et al. [15] showed that the burn rate of nSi-based energetic composites is strongly dependent on the equivalence ratio and oxidizer used. Recently, Si quantum dots prepared by fracturing porous silicon films were shown to retain the critical combustion properties of porous silicon [16]. As an additive, nSi was also shown to lower the ignition temperature and enhance the combustion performance of aluminum-based energetic composites [17,18].

Despite being in different forms, previously studied nanoenergetic Si is invariably crystalline. Its non-crystalline counterpart, amorphous Si (*a*-Si), has yet to be investigated because of a lack of synthesis techniques that can easily produce this material in nanoparticle form. *a*-Si lacks a periodically arranged atomic structure and is characterized by

* Corresponding authors.
E-mail address: lmangolini@engr.ucr.edu (M.R. Zachariah).

https://doi.org/10.1016/j.cej.2021.133140
Received 16 July 2021; Received in revised form 16 October 2021; Accepted 19 October 2021
Available online 29 October 2021
1385-8947/

the presence of dangling bonds among other defects. In most cases where silane is used as a precursor, plasma-synthesized *a*-Si nanoparticles are also hydrogenated via the incorporation of H atoms in the discharge. This feature resembles the H-terminated surface of PS, making *a*-Si nanoparticles a promising candidate for nanoenergetic applications. In addition, previous works on nanoenergetic Si mainly studied the effects of particle size, pore size, surface area, porosity, formulation, etc. on energetic performance, but the influence of silicon crystallinity has yet been reported.

In this work, we systematically investigate the energetic characteristics of Si nanoparticles (nSi) with emphasis on its amorphous form. A non-thermal plasma method was used to prepare uniform sub-10 nm Si particles [19]. In particular, we leverage the capability of this approach to control the degree of crystallinity of the particles by changing the level of the power coupled into the plasma discharge [20]. Comprehensive characterizations were carried out to reveal the differences in physicochemical properties between amorphous and crystalline nSi. The energetic characteristics of nSi when reacting with $KClO_4$ were evaluated using a combustion cell. The results indicate that there is a correlation between the energetic performance and the hydrogen content of nanostructured Si. *a*-nSi composites show significantly higher pressurization rate than their crystalline counterparts, presumably because of an explosive reaction of H_2/O_2 mixture. Evidence of in situ release of hydrogen obtained from Temperature-jump time-of-flight mass spectrometry (T-Jump TOFMS) suggests that highly reactive Si dangling bonds are created by hydrogen desorption before ignition. A reaction mechanism is proposed based on the characterization results, which implies that hydrogen plays a dual role in enhancing the energetic performance of hydrogenated *a*-nSi.

2. Experimental section

2.1. Materials

Aluminum nanopowder (nAl, ~80 nm, 81% active mass) was purchased from Novacentrix. Potassium perchlorate ($KClO_4$) microparticles (~1 μm; see Figure S1) were prepared via aerosol spray pyrolysis at 423 K using commercial $KClO_4$ (Sigma Aldrich) as previously reported [21].

2.2. Plasma synthesis of nSi particles

Silicon nanoparticles were synthesized using silane precursor with a nonthermal plasma reactor as illustrated in Figure S2. The system comprised a 1″ quartz tube and two copper ring electrodes. The first electrode was connected to a radiofrequency power supply, and the second electrode was grounded. 200 sccm of an Argon-silane mixture (1.36% SiH_4 in Ar) was flown in the rector while the pressure was maintained at 465 Pa. nSi particles were produced using three different plasma powers: 10 W, 20 W and 50 W. The particles were collected downstream of the plasma volume by filtering.

2.3. Characterizations of nSi particles

The distribution, average and standard deviation of the particle diameter were characterized via transmission electron microscopy (TEM) (FEI Tecnai12 microscope; accelerating voltage of 200 kV) by measuring an ensemble of 100 nanoparticles using ImageJ software. The hydrogen surface termination of the synthesized nSi particles was characterized with a Fourier transform infrared (FTIR) spectrometer in ATR configuration (Thermo Scientific Nicolet iS50-FTIR). An environmental chamber was used to perform FTIR measurement in diffuse reflectance as a function of temperature (Harrick Scientific Products: Praying Mantis Diffuse Reflection Accessory and Praying Mantis High Temperature Reaction Chamber HVC-DRM-5; temperature range: 100 °C-900 °C).

The hydrogen content of nSi particles was measured with the thermal desorption spectroscopy (TDS) system depicted in Figure S3a. 50–60 mg of nSi particles were loaded into an alumina combustion boat and placed at the center of a furnace. A flow of 10 sccm of Argon gas was introduced in the system and maintained at a static pressure of 65 Pa. The temperature of the furnace was ramped from 25 °C to 1000 °C to induce thermal desorption of hydrogen from the material (constant heating rate of 4 °C min^{-1}). This was monitored by sampling through a 50 μm orifice, into a turbo-pumped stage onto which a residual gas analyzer (RGA) is mounted.

The contribution to the hydrogen signal at amu = 2 from the fragmentation of water was accounted for by first measuring the water signal at room temperature and recording the ratio between the signal at amu = 18 and amu = 2. This allows the removal of any contribution from water to the amu = 2 signal, summarized by the equation below.

$$P_{H_2}(T) = amu_2(T) - amu_{18}(T) * \left(\frac{amu_2(25^\circ C)}{amu_{18}(25^\circ C)}\right)$$

P_{H2} (T) was normalized to the Argon signal at amu = 40 (P_{Ar}), a stable reference during the measurement, as described by the following equation.

$$H_2\ signal = P_{H_2}(T)/P_{Ar}(T)$$

As depicted in Figure S3b, the value of the H_2 signal (T) shows a linear dependence on the hydrogen flow. The area under the H_2 signal (T) is therefore directly proportional to the amount of hydrogen released by the nSi sample during the annealing process (see Figure S3c). In order to enable a quantitative analysis of the hydrogen storage capacity of the material, the TDS was calibrated using 6 mg of $LiAlH_4$ (see Figure S3d; the material contains 10% hydrogen content by weight). In the figures reported in the manuscript the H_2 signal (T) is normalized to the weight of the silicon powder used in the measurement.

2.4. Combustion cell characterizations of nSi/$KClO_4$ composites

Stoichiometric mixtures of nSi and $KClO_4$ particles were first dispersed in hexane and sonicated for 30 min. The suspension was then dried in air following which 25 mg of the prepared powder mixture was placed in a constant-volume (~20 cm^3) combustion cell [22], and ignited with a joule heated nichrome coil. The combustion cell was coupled with a high frequency pressure transducer (PCB Piezoelectronics) and a photomultiplier tube (Hamamatsu) to collect temporal pressure and optical signals, respectively. The pressure and optical signals were recorded simultaneously by an oscilloscope. The flame temperature measurement is detailed in the work by Jacob et al. [18] Briefly, the light emitted from the reaction is collected with an optical fiber, to a spectrometer (Acton SP 500i) coupled with a 32-channel photomultiplier (Hamamatsu, H7260) and a data acquisition system (Vertilon IQSP580). The collected spectral data was linearized according to Wein's law under grey body assumption. It was then plotted against the wavelength and the temperature was calculated by linear fitting.

2.5. Temperature-jump time resolved mass spectrometry and high-speed imaging

Temperature-jump time-of-flight mass spectrometry (T-Jump TOFMS) [23,24] was used to investigate Si/$KClO_4$ reaction at high heating rates. For a typical measurement, the sample powder was dispersed in hexane via sonication, and coated on a ~ 1 cm platinum wire (d = 76 μm) with a micropipette. During the measurement, the Pt wire was resistively heated to ~ 1400 K at ~ 10^5 K/s, and time resolved mass spectra were collected every 100 μs. The temperature of the wire can be determined by Callendar–Van Dusen equation from the I-V curve of the wire recorded by an oscilloscope. The ignition event was captured by a Vision Research Phantom v12.0 digital camera (frame rate = 100000 fps, exposure = 9.57 μs) from the observation window to

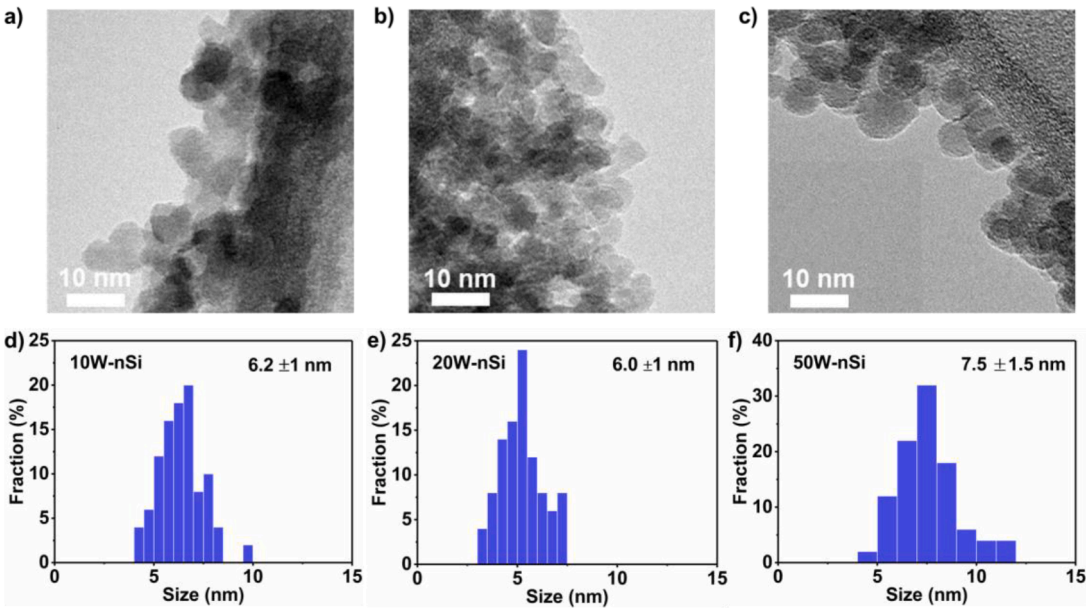

Fig. 1. TEM images of (a) 10 W, (b) 20 W and (c) 50 W-nSi. Size distributions of (d) 10 W, (e) 20 W and (f) 50 W-nSi obtained from TEM.

Table 1
Summary of chemical and physical characteristics of nSi particles.

Plasma power (W)	Silicon Phase	Particle size (nm)	SSA_{BET} ($m^2 \cdot g^{-1}$)	Active content (wt %)
10	Amorphous	6.2 ± 1	448.9	82.5
20	Amorphous	6.0 ± 1	454.5	81.6
50	Crystalline	7.5 ± 1.5	299.4	87.7

determine the ignition time.

3. Results and discussion

3.1. Synthesis and characterizations of nSi particles

In the present study, three different nSi particles were synthesized at plasma powers of 10 W, 20 W and 50 W, respectively. Particles formed in a non-thermal plasma are typically negatively charged, which reduces agglomeration and coalescence [25]. As a result, particles of ultra-small size and narrow size distribution can be prepared. Fig. 1a-c depicts TEM characterization of these materials. The 10 W-nSi and 20 W-nSi appear to be particles with quasi-spherical morphology while the 50 W-nSi comprises spherical particles. High resolution TEM of 10 W-nSi (Figure S4) shows no sign of crystal ordering, as confirmed by the Fast Fourier Transform (FFT). The particle size distributions of the three materials are shown in Fig. 1d-f. The average particle size of 10 W, 20 W and 50 W-nSi is 6.2 nm ± 1 nm, 6.0 nm ± 1 nm and 7.5 nm ± 1.5 nm, respectively. The nano-sized particles clearly offer a large surface area as determined by BET measurements (Table 1).

The crystallinity of nSi particles was characterized by XRD. As shown in Fig. 2a, 50 W-nSi exhibits pronounced peaks that can be indexed to (111), (220) and (311) planes of Si. By contrast, the 20 W-nSi and 10 W-nSi only show very broad features expected for amorphous silicon [20]. The broadening and weakening of the peaks suggest that the crystallinity of nSi decreases with reduced plasma power [20,26].

As previously mentioned, Si particles prepared from silane usually contain hydrogen. FTIR spectra (Figure S5) confirm that all the nSi particles incorporate silicon hydrides as evidenced by the peaks in SiH_x (x = 1,2,3) stretching region [27]. Fig. 2b shows an example spectrum of 10 W-nSi, with a prominent peak around 2100 cm^{-1}, and a doublet around 900 cm^{-1}. The peak around 2100 cm^{-1} is attributed to SiH_x stretching modes [27]. The deconvoluted SiH_x stretching region using Gaussian line shapes (Fig. 2b inset) shows contributions from SiH (~2091 cm^{-1}), SiH_2 (~2113 cm^{-1}) and SiH_3 (~2143 cm^{-1}) [28]. The doublet around 900 cm^{-1} is associated with the bending and wagging deformation modes of SiH_2 and SiH_3 [29]. Moreover, the absence of bulk SiH stretching vibration absorption band at ~ 2000 cm^{-1} suggests that most hydrides are on the surface of nSi particles [30].

Thermal desorption spectroscopy (TDS) was performed to study the evolution of hydrogen and quantify the hydrogen content in nSi particles. As shown in Fig. 2c, hydrogen signals of all three samples are composed of a principal peak and a smaller shoulder. To obtain accurate peak parameters, Gaussian deconvolution of the signals (dashed lines in Fig. 2c and Figure S6) are shown. The principal peak of 50 W *c*-nSi is centered around 377 °C and the associated shoulder is centered around 450 °C. For *a*-nSi samples, both peaks shift to slightly lower temperatures. A combined TDS and FTIR study by Rivolo et al. [31] showed a similar desorption behavior in hydrogenated silicon. Their results indicated that the principal peak corresponds to H_2 desorption from SiH_2/SiH_3, and the shoulder corresponds to H_2 desorption from SiH. This temperature dependent evolution of hydrogen was verified by performing in-situ FTIR measurements as a function of temperature (Figure S7). Based on the above information, hydrogen content was estimated quantitatively by integration of the deconvoluted TDS signals, yielding hydrogen atomic percentages of 33%, 26% and 17% for 10 W, 20 W and 50 W-nSi, respectively. By comparing the integrated peak areas of the two isolated peaks, the amount of hydrogen desorbed from monohydride and higher hydride species was also determined. The results are shown in Fig. 2d. It is clear that total hydrogen content decreases as the sample becomes more crystalline, mainly because of less SiH_2 and SiH_3 surface moieties compared to SiH. This is likely due to the higher temperature related to the formation of more crystalline nSi particles in the plasma environment [25]. The material crystallization mechanism in the plasma reactor is driven by energetic surface reactions that bring the particle temperature above the crystallization threshold [32]. On the other hand, for amorphous materials such as 10 W-nSi and 20 W-nSi, the plasma power level is too low for particle-heating to induce crystallization [25].

Simultaneous thermalgravimetric analysis and differential scanning calorimetry (TGA/DSC) was used to study the thermal oxidation of nSi particles. Measurements were performed from room temperature to 1000 °C at a ramp rate of 20 °C min^{-1} in O_2 atmosphere. The active

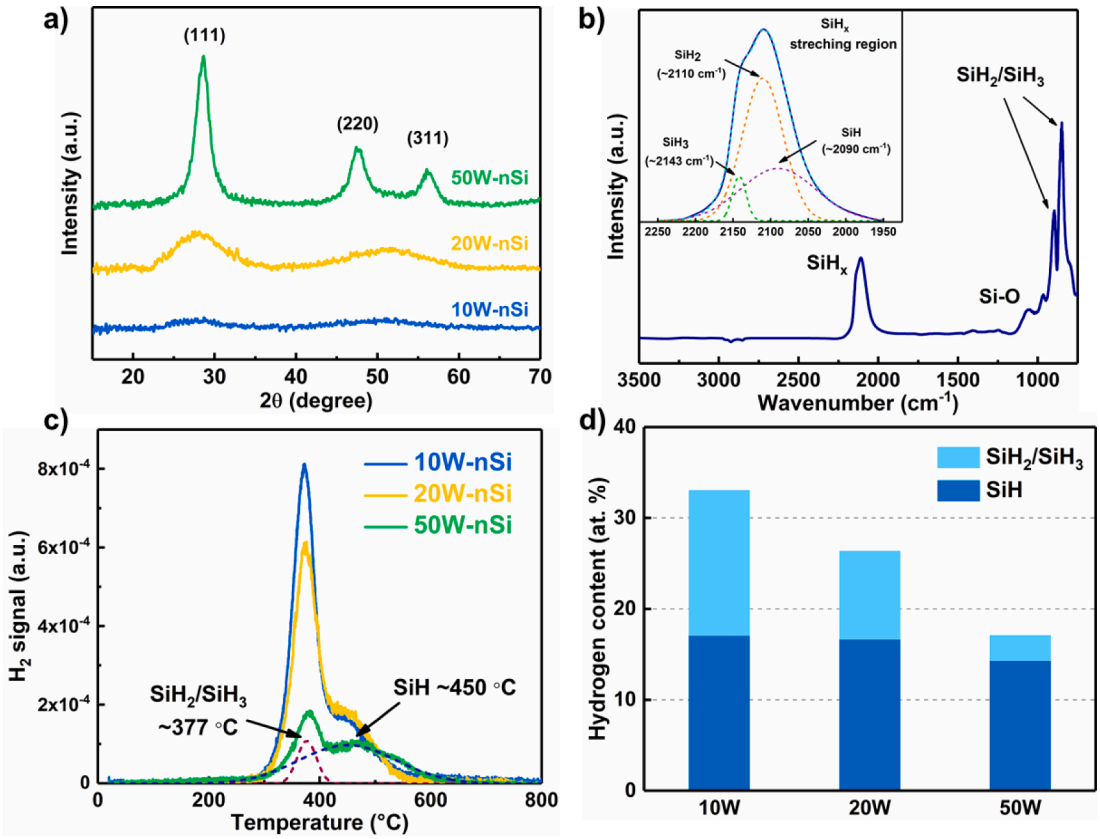

Fig. 2. (a) XRD patterns of 10 W, 20 W and 50 W-nSi. The broadening and weakening of the peaks indicate decreased crystallinity. (b) FTIR spectrum of 10 W-nSi showing SiH_x stretching region near 2100 cm^{-1} and SiH_2/SiH_3 deformation region near 900 cm^{-1}. Inset: SiH_x stretching region deconvoluted using Gaussian line shapes. (c) TDS spectra of 10 W, 20 W and 50 W-nSi. The principal peak and the shoulder peak correspond to hydrogen desorption from higher hydrides and monohydride, respectively. Gaussian deconvolution of the 50 W-nSi spectrum is shown as dashed lines. (d) Hydrogen content of different nSi and its composition. The difference in hydrogen content among nSi samples mainly lies in higher hydride species.

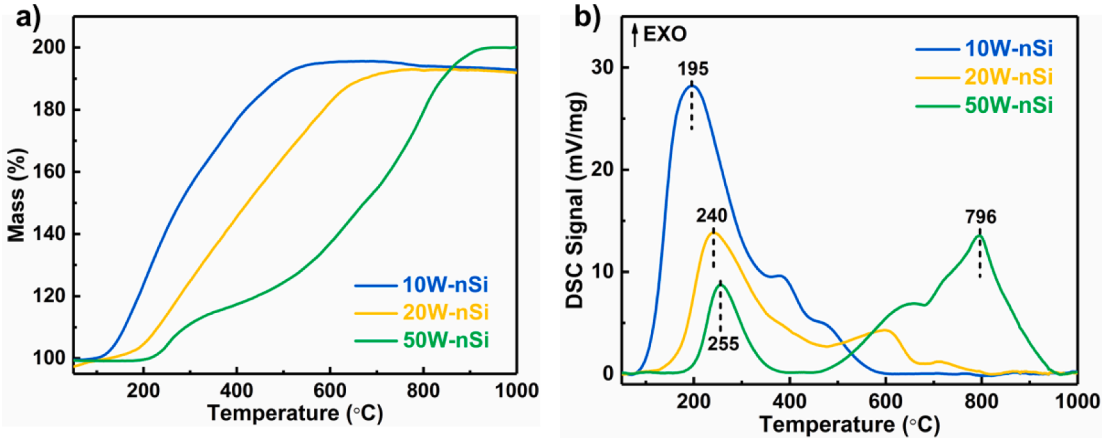

Fig. 3. Mass change and corresponding DSC signals of nSi measured in O_2 at 20 K min^{-1}. *a*-nSi shows higher oxidation rate and a major exothermic peak at low temperature.

content of nSi particles (Table 1) was obtained from the mass increase in TGA after complete oxidation. As shown in Fig. 3a, both the onset and completion temperatures of nSi oxidation follow the order 10 W < 20 W < 50 W, indicating that *a*-nSi is more susceptible to oxidation than *c*-Si. DSC signals in Fig. 3b also show a unique pattern for each nSi sample. 10 W and 20 W *a*-nSi show a major exothermic peak at around 195 °C and 240 °C, respectively. By contrast, 50 W *c*-nSi shows a moderate exothermic peak at ~ 300 °C and a major exothermic peak at ~ 800 °C. The classic linear-parabolic model proposed by Deal and Grove describes very well the thermal oxidation of thick silicon films [33]. However, it does not account for oxide growth in the thin film regime of hundreds of angstroms [34]. Liao et al. [35] reported two regimes of thermal oxidation of plasma-synthesized *c*-Si nanoparticles. The first regime is the fast oxidation of the surface via direct contact with oxygen. After surface oxidation, an oxide layer which hinders oxygen diffusion will form, and oxidation becomes diffusion limited. The second regime is the diffusion-controlled growth of the oxide layer at elevated temperature. This description matches the oxidation pattern of 50 W-nSi that is

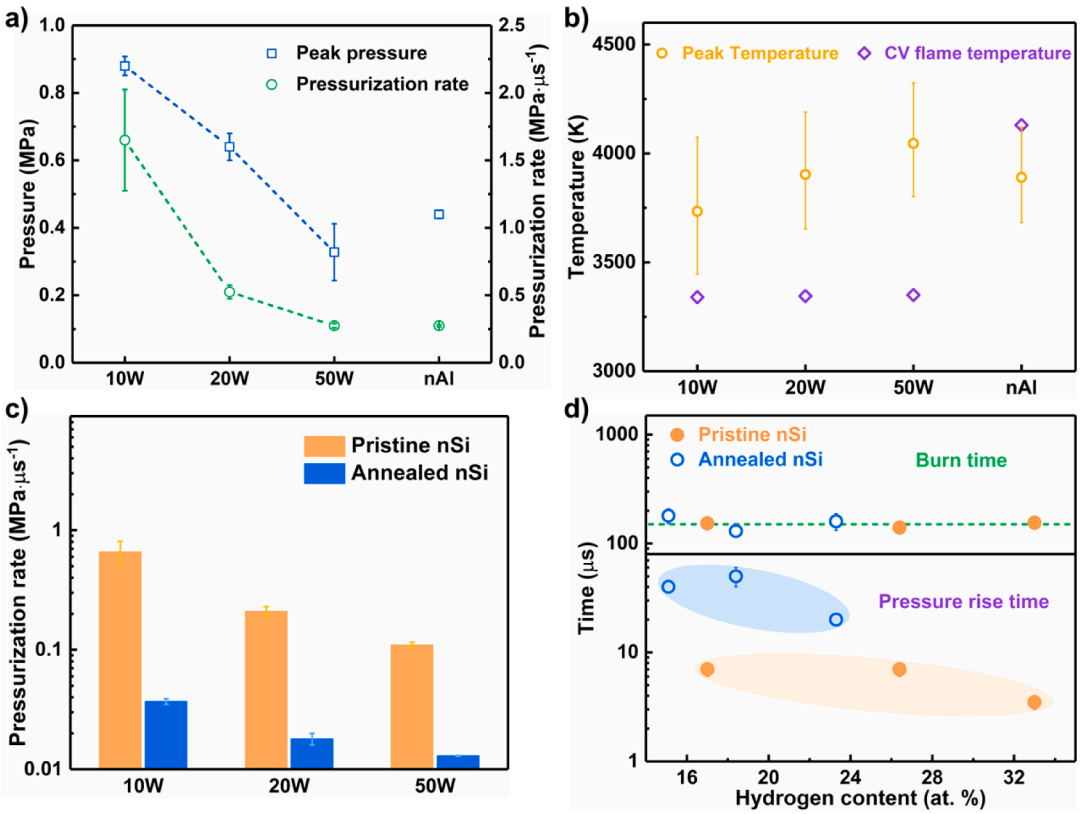

Fig. 4. Combustion cell measurement results of nSi/$KClO_4$ and nAl/$KClO_4$ composites. (a) Peak pressure and pressurization rate. (b) Measured and calculated constant volume (CV) flame temperature. (c) Comparison of pressurization rate of nSi/$KClO_4$ composites prepared with pristine and annealed nSi. Annealed nSi particles are partially dehydrogenated. (d) Optically determined burn time and pressure rise time of nSi/$KClO_4$ composites prepared with pristine and annealed nSi. The burn time remains the same after annealing while the pressure rise time decreases by one order of magnitude.

also crystalline. However, for 10 W and 20 W *a*-nSi samples, oxidation seems to occur mainly in the first regime and the second regime at elevated temperature is missing. The low temperature oxidation regime is likely related to the backbond oxidation of surface silicon hydrides [36] and oxidation promoted by hydrogen desorption [34]. This hypothesis is validated by the diminishing low temperature exothermic peak as the hydrogen content decreases in the samples. Potential structural defects in *a*-Si [37], which provide pathway for oxygen permeation, may also contribute to the facile oxidation of *a*-nSi particles.

3.2. *Energetic characteristics of nSi/$KClO_4$ composites*

In order to investigate the combustion characteristics of nSi, nSi and $KClO_4$ particles were homogeneously mixed to form composites. $KClO_4$ was selected as the oxidizer because perchlorate salts have been shown to be very effective oxidizers in porous Si based energetic composites. The combustion experiments of nSi/$KClO_4$ composites were carried out in a constant-volume combustion cell (20 ml) [22], from which peak pressure, pressurization rate (dP/dt), burn time can be extracted.

The pressure history of 10 W-nSi/$KClO_4$, 20 W-nSi/$KClO_4$, 50 W-nSi/$KClO_4$ and nAl/$KClO_4$ composites are shown in Figure S8. nAl serves as a reference to gauge the performance of nSi. All samples show a rapid pressure rise and reach a peak pressure except for 50 W-nSi composite, whose pressure continues to climb slightly after the initial pressure rise. For comparison purposes, the initial pressure rise was used for calculating peak pressure and pressurization rate. The peak pressures and pressurization rates are shown in Fig. 4a. Both peak pressure and pressurization rate decrease with increasing crystallinity of nSi. 10 W-nSi/$KClO_4$ has the highest peak pressure (2.2 MPa) and pressurization rate (0.66 MPa·μs^{-1}), which increases by a factor of two and six compared to that of nAl/$KClO_4$, respectively. The results demonstrate that *a*-nSi composites are superior to nAl composite in terms of pressure generation.

The flame temperature of nSi/$KClO_4$ composites (~3700–4000 K) measured in combustion cell is comparable to that of nAl/$KClO_4$ composite (~3900 K), as shown in Fig. 4b. *c*-nSi shows slightly higher flame temperature. The constant volume (CV) adiabatic flame temperature of Si/$KClO_4$ with added hydrogen was also calculated using the CHEETAH thermochemical code. The results indicate that additional hydrogen does not have any substantial effects on the adiabatic flame temperature.

It is apparent from the pressure cell results that *a*-nSi composites perform better than *c*-nSi composites with respect to pressure generation. One may naturally relate the improvement in gas output to higher hydrogen content in *a*-nSi. To validate this hypothesis, annealing experiments were performed at 350 ℃ in vacuum to partially remove hydrogen from nSi particles. XRD patterns of annealed nSi (Figure S9a) confirm that 10 W and 20 W-nSi are still amorphous. According to the TDS results, at 350 ℃, H_2 desorption from higher hydride species (SiH_2/SiH_3) should occur. As shown in Figure S9b, the drop in hydrogen content of annealed nSi particles is consistent with the estimated amount of hydrogen from higher hydrides in the pristine nSi particles. The desorption of hydrogen may cause reconstruction of the nSi surface [38]. BET measurements (Figure S9c) indicate that the specific surface area of 10 W and 20 W-nSi slightly decreases after annealing, but no significant change was observed for 50 W-nSi. The characterizations of annealed nSi particles suggest that their respective amorphous and crystalline characteristics are largely retained apart from being partially dehydrogenated.

Compared to pristine nSi, the annealed nSi leads to one order of magnitude decrease in the pressurization rate of nSi/$KClO_4$ composites,

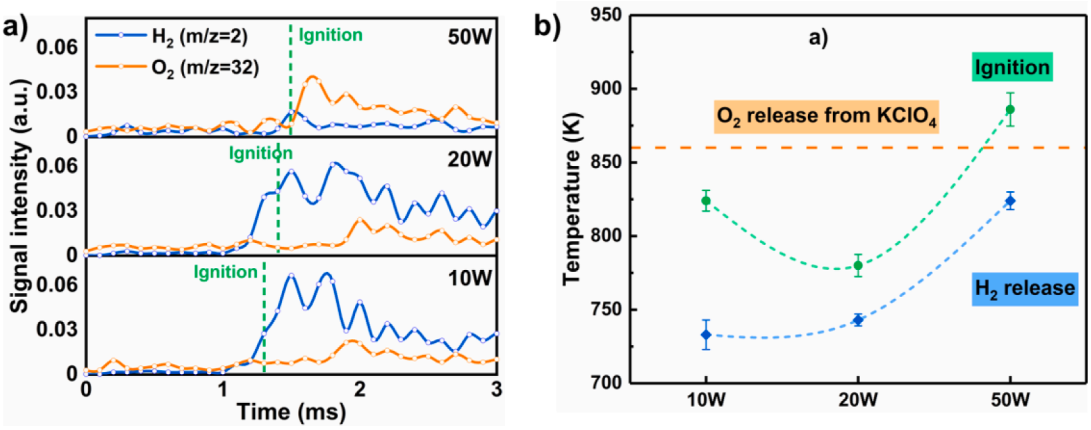

Fig. 5. (a) Temporal signals of H_2 and O_2 from nSi/$KClO_4$ T-jump mass spectrometry. (b) Ignition and H_2 release temperature of nSi/$KClO_4$. The horizontal dashed line represents O_2 release temperature from $KClO_4$ decomposition.

as shown in Fig. 4c. The decreased pressurization rate of annealed nSi composites suggests that the enhanced energetic characteristics are due to hydrogen incorporated in nSi. Shown in Fig. 4d are the burn times and pressure rise times of nSi/$KClO_4$ composites before and after annealing. The full width at half maximum (FWHM) of the optical signal was taken as a measure of the burn time. All samples, including annealed ones, have similar burn times ($\sim 10^{-4}$ s) despite their distinctly different pressurization rates. The pressure rise time of annealed nSi composites ($\sim 10^{-5}$ s) is one order of magnitude longer than that of pristine ones ($\sim 10^{-6}$ s), although they are both significantly shorter than the optically determined burn time. The disparity between burn time and pressure rise time indicate that the occurrences of rapid gas generation and particle burning are not simultaneous. The pressure output of nSi composites depends primarily on a rapid event that occurs at the start of the reaction rather than the relatively slow burning of nSi particles. The rapid pressure rise could be a result of the facile decomposition of the oxidizer, according to Sullivan et al. [39] However, that is unlikely the case here because the high pressurization rate is not seen in *c*-nSi or nAl composites with the same oxidizer. It is not a direct consequence of hydrogen release from nSi either, because even for 10 W-nSi with the highest hydrogen content, the upper limit of the pressure that the released H_2 can generate is about 76 kPa, which does not even remotely account for the increase in the peak pressure (~1000 kPa) compared to that of 50 W-nSi composite.

The surface chemistry of nSi particles resembles closely that of porous silicon, which has been shown to react explosively with various oxidizers. Kovalev et al. [40] reported an explosive reaction between hydrogenated porous silicon and oxygen at cryotemperatures. The explosion is believed to initiate with an exothermic reaction between silicon dangling bonds and oxygen, and propagate via a hydrogen–oxygen and silicon-oxygen branched chain reaction. Churaman et al. [41] reported the formation of O and OH radicals during the explosion of porous silicon impregnated with $NaClO_4 \bullet H_2O$, and proposed a chain reaction mechanism based on Quantum Rice-Ramsperger-Kassel (QRRK) theory. In the present study, given the large surface area with abundant hydride species, it is reasonable to expect that similar reactions can occur in the nSi/$KClO_4$ system. We also should note that the reported time scale of the porous silicon explosive reaction [38] is of the same time scale as the pressure rise (10^{-6} s) in this study, which further supports our interpretation.

3.3. *Mechanistic investigation of nSi/$KClO_4$ reaction by T-Jump TOFMS*

To establish a more comprehensive understanding on the reaction mechanism, Temperature-jump time-of-flight mass spectrometry (T-jump TOFMS) was used to investigate the reaction between nSi and $KClO_4$. T-jump TOFMS simulates the high heating rate ($\sim 5x10^5$ K/s) during nanoenergetic reactions and collects mass spectra of evolved species with a temporal resolution of 0.1 ms. Selected time-resolved mass spectra of nSi/$KClO_4$ ignition are shown in Figure S10. Typically, the background of the spectra mainly consists of H_2O ($m/z = 18$) O_2 ($m/z = 16$) and N_2 ($m/z = 14$). As time evolves, H_2 ($m/z = 2$), SiH ($m/z = 29$), SiH_2 ($m/z = 30$) and SiH_3 ($m/z = 31$) signals start to appear, most prominently in *a*-nSi composites, representing the onset of hydrogen and silicon hydrides desorption. O_2 and K^+ ($m/z = 39$) signals from $KClO_4$ decomposition can also be observed afterward.

Hydrogen release is an important step for ignition because as a passivation layer, hydrogen can either enhance the reactivity by readily exposing silicon dangling bonds or hinder the reaction by acting as a barrier between oxygen and silicon. To further understand the role of hydrogen during reaction, temporal signals of H_2 and O_2 from different samples are plotted in Fig. 5a. These measurements were performed under similar conditions and thus can be analyzed in a semiquantitative manner. As illustrated in Fig. 5a, going from 10 W to 50 W samples, the peak intensity of H_2 signals gradually decreases while the peak intensity of O_2 signals increases. Noticeably, both *a*-nSi composites have H_2 peaks that are more pronounced than O_2 peaks, while *c*-nSi composite shows the opposite. Stronger H_2 signals from *a*-nSi composites are expected as *a*-nSi contains more hydrogen. However, the explanation for decreased O_2 peak intensity in *a*-nSi composites is less intuitive. In the nSi/$KClO_4$ reaction, O_2 comes from the decomposition of $KClO_4$. The mass percentage of $KClO_4$ in each mixture is the same and *a*-nSi is not likely to inhibit O_2 release from $KClO_4$. An alternative explanation is that the released O_2 is consumed before it can escape the reaction zone. As previously discussed, this could be a result of released oxygen reacting with Si dangling bonds created after hydrogen/hydrides desorption. This hypothesis is further supported by the higher hydrogen content and lower H_2 release temperature of *a*-nSi composites (Fig. 5b), which provides more Si dangling bonds after desorption and increases the rate of reaction with oxygen, leading to diminished oxygen peaks. On the other hand, 50 W-nSi composite has an intense O_2 peak with a prolonged tail. This implies that $KClO_4$ produces a large amount of gaseous oxygen after ignition, followed by nSi particles burning slowly in oxygen. The difference in combustion behavior between amorphous and crystalline nSi composites is also reflected by the high-speed images of nSi/$KClO_4$ ignition (Figure S11). For 10 W and 20 W nSi composites, the reaction zone is visually larger than 50 W nSi composite with particles ejected from the wire, suggesting more violent reactions with significant gas generation.

Fig. 5b shows the ignition and H_2 release temperature of nSi composites, along with oxygen release temperature of bare $KClO_4$. The H_2 release temperature of *a*-nSi composites is about 90 K lower than that of

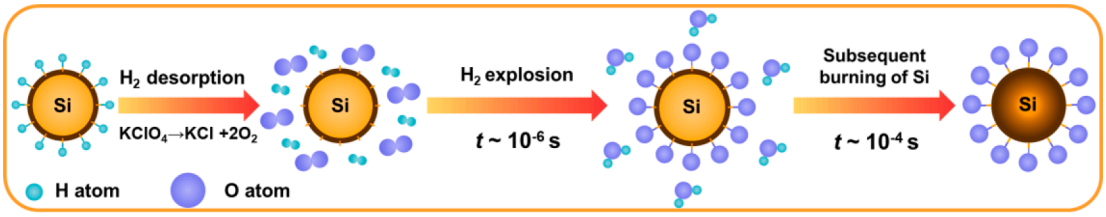

Fig. 6. Schematic illustration of the proposed reaction mechanism of nSi/$KClO_4$ composites.

c-nSi composite, because *a*-nSi contains more SiH_2/SiH_3 species that has a lower desorption temperature. The ignition temperature of *a*-nSi composites is also lower than that of *c*-nSi composite. It is even lower than the oxygen release temperature of $KClO_4$, implying that silicon dangling bonds might react with nascent oxygen from $KClO_4$ decomposition. By contrast, the ignition temperature of 50 W *c*-nSi composite is slightly higher than the decomposition temperature of $KClO_4$, possibly because the ignition requires higher oxygen concentration for lack of Si dangling bonds. It is somewhat unanticipated that 20 W-nSi composite has the lowest ignition temperature among the three samples. We are unsure about the reason, but it is worth noting that 20 W-nSi also has the smallest size and largest surface area.

As demonstrated by the T-jump mass spectroscopy results, H_2 and O_2 are released during the reaction. In the mass spectrometer, because of the high vacuum environment and short residence time in the reaction zone, further reactions between H_2 and O_2 are unlikely to happen. However, in the previous constant-volume combustion cell experiments, the rapid pressure rise observed for *a*-nSi composites could be a result of the explosion of H_2/O_2 mixture, as H_2 is known to have a broad range of explosion limit and requires very little energy to ignite. Taking 10 W-nSi for example, the gas composition in the combustion cell after H_2 release can be considered as a H_2/O_2 mixture diluted with N_2. Depending on the extent of $KClO_4$ decomposition, the volume concentration of H_2 varies from 4.4 to 5.6%, which is above the 4% lower explosive limit (LEL) of H_2/O_2 mixture. It is valid to use the LEL for H_2/O_2 mixture here because N_2 dilution, up to 85%, has been shown to only increase LEL by 0.25% [42]. The minimum ignition energy (MIE) for the H_2 mixture in the combustion cell can be reasonably assumed to be ~ 1 mJ, as reported for fuel lean H_2 mixtures [43,44]. The MIE for H_2 explosion is about 0.0005% of the estimated heat release from Si/$KClO_4$ reaction (~220 J) in the combustion cell. As a result, it is most likely that H_2 explosion occurs and results in the high pressurization rate.

Based on the above discussions, a reaction mechanism explaining the high reactivity of *a*-nSi/$KClO_4$ composites is proposed and illustrated in Fig. 6. For hydrogenated *a*-Si, hydrogen from higher hydrides first starts to desorb upon heating, leaving behind Si dangling bonds. Immediately after, $KClO_4$ starts to decompose and liberates oxygen. When oxygen comes into contact with Si dangling bonds, exothermic reaction occurs immediately and leads to ignition. The explosion of H_2/O_2 mixture most likely leads to the very high pressurization rate in the combustion cell. This process occurs on a time scale of 10^{-6} s as estimated from the pressure rise time. However, the optically determined burn time is ~ 10^{-4} s, implying that the nSi particles continue to burn after the initial H_2/O_2 explosive reaction.

4. Conclusions

In summary, we have discussed the energetic characteristics of amorphous and crystalline nSi particles prepared by a non-thermal plasma. *a*-nSi with a high hydrogen content demonstrates enhanced pressure output in combustion cell measurements over *c*-nSi when formulated with $KClO_4$. The pressurization rate of 10 W *a*-nSi/$KClO_4$ composite increases by a factor of six compared with nAl to 0.66 $MPa{\cdot}\mu s^{-1}$. The dual role of hydrogen in improving the energetic performance is proposed: 1) the facile release of hydrogen from *a*-nSi before ignition, as confirmed by time-resolved T-jump mass spectrometry, leaves behind highly reactive Si dangling bonds which ignite instantly when contact with oxygen. 2) The desorbed H_2 likely reacts with O_2 explosively, leading to the high pressurization rate. The enhanced energetic performance of hydrogenated *a*-nSi indicates that incorporation of hydrogen could be a promising strategy for improving the performance of nanoenergetic composites.

Declaration of Competing Interest

The authors declare that they have no known competing financial interests or personal relationships that could have appeared to influence the work reported in this paper.

Acknowledgement

This work was supported by the DTRA-Materials Science under Extreme Conditions URA.

Appendix A. Supplementary data

Supplementary data to this article can be found online at https://doi.org/10.1016/j.cej.2021.133140.

References

[1] B.F.P. McVey, R.D. Tilley, Solution Synthesis, Optical Properties, and Bioimaging Applications of Silicon Nanocrystals, Acc. Chem. Res. 47 (10) (2014) 3045–3051, https://doi.org/10.1021/ar500215v.
[2] C.H. Yang, R.C.C. Leon, J.C.C. Hwang, A. Saraiva, T. Tanttu, W. Huang, J. Camirand Lemyre, K.W. Chan, K.Y. Tan, F.E. Hudson, K.M. Itoh, A. Morello, M. Pioro-Ladrière, A. Laucht, A.S. Dzurak, Operation of a silicon quantum processor unit cell above one kelvin, Nature 580 (7803) (2020) 350–354, https://doi.org/10.1038/s41586-020-2171-6.
[3] F. Priolo, T. Gregorkiewicz, M. Galli, T.F. Krauss, Silicon nanostructures for photonics and photovoltaics, Nature Nanotech. 9 (1) (2014) 19–32, https://doi.org/10.1038/nnano.2013.271.
[4] Y. Jin, B. Zhu, Z. Lu, N. Liu, J. Zhu, Challenges and Recent Progress in the Development of Si Anodes for Lithium-Ion Battery, Adv. Energy Mater. 7 (23) (2017) 1700715, https://doi.org/10.1002/aenm.v7.2310.1002/aenm.201700715.
[5] M.d. Plessis, A Decade of Porous Silicon as Nano-Explosive Material, Propellants Explos. Pyrotech. 39 (3) (2014) 348–364, https://doi.org/10.1002/prep.v39.310.1002/prep.201300053.
[6] M. Comet, C. Martin, F. Schnell, D. Spitzer, Nanothermites: A short Review, Factsheet for Experimenters, Present and Future Challenges, Propellants, Explosives, Pyrotechnics. 44 (1) (2019) 18–36, https://doi.org/10.1002/prep.v44.110.1002/prep.201800095.
[7] N.W. Piekiel, C.J. Morris, Small-Scale, Self-Propagating Combustion Realized with On-Chip Porous Silicon, ACS Appl. Mater. Interfaces. 7 (18) (2015) 9889–9897, https://doi.org/10.1021/acsami.5b01964.
[8] Y. Ohkura, J.M. Weisse, L. Cai, X. Zheng, Flash ignition of freestanding porous silicon films: effects of film thickness and porosity, Nano Lett. 13 (11) (2013) 5528–5533, https://doi.org/10.1021/nl403114g.
[9] N.W. Piekiel, C.J. Morris, W.A. Churaman, M.E. Cunningham, D.M. Lunking, L. J. Currano, Combustion and Material Characterization of Highly Tunable On-Chip Energetic Porous Silicon, Propellants Explos. Pyrotech. 40 (1) (2015) 16–26, https://doi.org/10.1002/prep.v40.110.1002/prep.201400140.
[10] P.M. Guerieri, B. Fuchs, W.A. Churaman, Feasibility of Detonation in Porous Silicon Nanoenergetics, Propellants Explos. Pyrotech. 46 (8) (2021) 1260–1275, https://doi.org/10.1002/prep.v46.810.1002/prep.202000311.
[11] A. Abraham, N.W. Piekiel, C.J. Morris, E.L. Dreizin, Combustion of Energetic Porous Silicon Composites Containing Different Oxidizers, Propellants Explos. Pyrotech. 41 (1) (2016) 179–188, https://doi.org/10.1002/prep.201500108.

[12] C.R. Becker, S. Apperson, C.J. Morris, S. Gangopadhyay, L.J. Currano, W. A. Churaman, C.R. Stoldt, Galvanic Porous Silicon Composites for High-Velocity Nanoenergetics, Nano Lett. 11 (2) (2011) 803–807, https://doi.org/10.1021/nl104115u.
[13] S. Huang, V.S. Parimi, S. Deng, S. Lingamneni, X. Zheng, Facile Thermal and Optical Ignition of Silicon Nanoparticles and Micron Particles, Nano Lett. 17 (10) (2017) 5925–5930, https://doi.org/10.1021/acs.nanolett.7b0175410.1021/acs.nanolett.7b01754.s001.
[14] R. Thiruvengadathan, G.M. Belarde, A. Bezmelnitsyn, M. Shub, W. Balas-Hummers, K. Gangopadhyay, S. Gangopadhyay, Combustion Characteristics of Silicon-Based Nanoenergetic Formulations with Reduced Electrostatic Discharge Sensitivity, Propellants Explos. Pyrotech. 37 (3) (2012) 359–372, https://doi.org/10.1002/prep.201100129.
[15] B.A. Mason, L.J. Groven, S.F. Son, R.A. Yetter, Combustion Performance of Several Nanosilicon-Based Nanoenergetics, J. Propul. Power 29 (6) (2013) 1435–1444, https://doi.org/10.2514/1.B34902.
[16] S.K. Adams, N.W. Piekiel, M.H. Ervin, C.J. Morris, Silicon quantum dots for energetic material applications, Appl. Phys. Lett. 112 (23) (2018) 233108, https://doi.org/10.1063/1.5022587.
[17] P. Ghildiyal, X. Ke, P. Biswas, G. Nava, J. Schwan, F. Xu, D.J. Kline, H. Wang, L. Mangolini, M.R. Zachariah, Silicon Nanoparticles for the Reactivity and Energetic Density Enhancement of Energetic-Biocidal Mesoparticle Composites, ACS Appl. Mater. Interfaces. 13 (1) (2021) 458–467, https://doi.org/10.1021/acsami.0c1715910.1021/acsami.0c17159.s001.
[18] F. Xu, P. Biswas, G. Nava, J. Schwan, D.J. Kline, M.C. Rehwoldt, L. Mangolini, M. R. Zachariah, Tuning the reactivity and energy release rate of I2O5 based ternary thermite systems, Combust. Flame 228 (2021) 210–217, https://doi.org/10.1016/j.combustflame.2020.12.047.
[19] L. Mangolini, E. Thimsen, U. Kortshagen, High-Yield Plasma Synthesis of Luminescent Silicon Nanocrystals, Nano Lett. 5 (4) (2005) 655–659, https://doi.org/10.1021/nl050066y.
[20] T. Lopez, L. Mangolini, Low activation energy for the crystallization of amorphous silicon nanoparticles, Nanoscale. 6 (3) (2014) 1286–1294, https://doi.org/10.1039/C3NR02526H.
[21] M.C. Rehwoldt, Y. Yang, H. Wang, S. Holdren, M.R. Zachariah, Ignition of Nanoscale Titanium/Potassium Perchlorate Pyrotechnic Powder: Reaction Mechanism Study, The Journal of Physical Chemistry C. 122 (20) (2018) 10792–10800, https://doi.org/10.1021/acs.jpcc.8b0316410.1021/acs.jpcc.8b03164.s001.
[22] R.J. Jacob, D.J. Kline, M.R. Zachariah, High speed 2-dimensional temperature measurements of nanothermite composites: Probing thermal vs. Gas generation effects, J. Appl. Phys. 123 (11) (2018) 115902, https://doi.org/10.1063/1.5021890.
[23] L. Zhou, N. Piekiel, S. Chowdhury, M.R. Zachariah, T-Jump/time-of-flight mass spectrometry for time-resolved analysis of energetic materials, Rapid Commun Mass Spectrom. 23 (1) (2009) 194–202, https://doi.org/10.1002/rcm.v23:110.1002/rcm.3815.
[24] G. Jian, N.W. Piekiel, M.R. Zachariah, Time-Resolved Mass Spectrometry of Nano-Al and Nano-Al/CuO Thermite under Rapid Heating: A Mechanistic Study, The Journal of Physical Chemistry C. 116 (51) (2012) 26881–26887, https://doi.org/10.1021/jp306717m.
[25] U.R. Kortshagen, R.M. Sankaran, R.N. Pereira, S.L. Girshick, J.J. Wu, E.S. Aydil, Nonthermal Plasma Synthesis of Nanocrystals: Fundamental Principles, Materials, and Applications, Chem. Rev. 116 (18) (2016) 11061–11127, https://doi.org/10.1021/acs.chemrev.6b00039.
[26] G. Nava, F. Fumagalli, S. Gambino, I. Farella, G. Dell'Erba, D. Beretta, G. Divitini, C. Ducati, M. Caironi, A. Cola, F. Di Fonzo, Towards an electronic grade nanoparticle-assembled silicon thin film by ballistic deposition at room temperature: the deposition method, and structural and electronic properties, J. Mater. Chem. C. 5 (15) (2017) 3725–3735, https://doi.org/10.1039/C7TC00187H.
[27] J. Holm, J.T. Roberts, Surface Chemistry of Aerosolized Silicon Nanoparticles: Evolution and Desorption of Hydrogen from 6-nm Diameter Particles, J. Am. Chem. Soc. 129 (2007) 2496–2503, https://doi.org/10.1021/ja0658970.
[28] B. Bardet, D. De Sousa Meneses, T. Defforge, J. Billoué, G. Gautier, In situ investigation of mesoporous silicon oxidation kinetics using infrared emittance spectroscopy, Phys Chem Chem Phys. 18 (27) (2016) 18201–18208, https://doi.org/10.1039/C6CP02086K.
[29] D.C. Marra, E.A. Edelberg, R.L. Naone, E.S. Aydil, Silicon hydride composition of plasma-deposited hydrogenated amorphous and nanocrystalline silicon films and surfaces, J. Vac. Sci. Technol., A 16 (6) (1998) 3199–3210, https://doi.org/10.1116/1.581520.
[30] B.N. Jariwala, N.J. Kramer, M.C. Petcu, D.C. Bobela, M.C.M.V.d. Sanden, P. Stradins, C.V. Ciobanu, S. Agarwal, Surface Hydride Composition of Plasma-Synthesized Si Nanoparticles, J. Phys. Chem. C. 115 (42) (2011) 20375–20379, https://doi.org/10.1021/jp2028005.
[31] P. Rivolo, F. Geobaldo, M. Rocchia, G. Amato, A.M. Rossi, E. Garrone, Joint FTIR and TPD study of hydrogen desorption from p+-type porous silicon, Physica Status Solidi (a). 197 (2003) 217–221, https://doi.org/10.1002/pssa.200306503.
[32] N.J. Kramer, R.J. Anthony, M. Mamunuru, E.S. Aydil, U.R. Kortshagen, Plasma-induced crystallization of silicon nanoparticles, J. Phys. D Appl. Phys. 47 (7) (2014) 075202, https://doi.org/10.1088/0022-3727/47/7/075202.
[33] B.E. Deal, A.S. Grove, General Relationship for the Thermal Oxidation of Silicon, J. Appl. Phys. 36 (12) (1965) 3770–3778, https://doi.org/10.1063/1.1713945.
[34] M. Vazquez-Pufleau, A Simple Model for the High Temperature Oxidation Kinetics of Silicon Nanoparticle Aggregates, Silicon. 13 (1) (2021) 189–200, https://doi.org/10.1007/s12633-020-00415-3.
[35] Y.-C. Liao, A.M. Nienow, J.T. Roberts, Surface Chemistry of Aerosolized Nanoparticles: Thermal Oxidation of Silicon, J. Phys. Chem. B. 110 (12) (2006) 6190–6197, https://doi.org/10.1021/jp054195e10.1021/jp054195e.s001.
[36] M.Y. Bashouti, K. Sardashti, J. Ristein, S.H. Christiansen, Early stages of oxide growth in H-terminated silicon nanowires: determination of kinetic behavior and activation energy, Phys. Chem. Chem. Phys. 14 (34) (2012) 11877, https://doi.org/10.1039/c2cp41709j.
[37] W. Beyer, W. Hilgers, P. Prunici, D. Lennartz, Voids in hydrogenated amorphous silicon materials, J. Non-Cryst. Solids 358 (17) (2012) 2023–2026, https://doi.org/10.1016/j.jnoncrysol.2011.09.030.
[38] P. Gupta, V.L. Colvin, S.M. George, Hydrogen desorption kinetics from monohydride and dihydride species on silicon surfaces, Phys. Rev. B. 37 (14) (1988) 8234–8243, https://doi.org/10.1103/PhysRevB.37.8234.
[39] K. Sullivan, M. Zachariah, Simultaneous Pressure and Optical Measurements of Nanoaluminum Thermites: Investigating the Reaction Mechanism, J. Propul. Power 26 (3) (2010) 467–472, https://doi.org/10.2514/1.45834.
[40] D. Kovalev, V.Y. Timoshenko, N. Künzner, E. Gross, F. Koch, Strong Explosive Interaction of Hydrogenated Porous Silicon with Oxygen at Cryogenic Temperatures, Phys. Rev. Lett. 87 (2001), 068301, https://doi.org/10.1103/PhysRevLett.87.068301.
[41] W. Churaman, L. Currano, A.K. Singh, U.S. Rai, M. Dubey, P. Amirtharaj, P.C. Ray, Understanding the high energetic behavior of nano-energetic porous silicon, Chem. Phys. Lett. 464 (4-6) (2008) 198–201, https://doi.org/10.1016/j.cplett.2008.09.017.
[42] X. Hu, Q. Xie, J. Zhang, Q. Yu, H. Liu, Y. Sun, Experimental study of the lower flammability limits of H2/O2/CO2 mixture, Int. J. Hydrogen Energy 45 (51) (2020) 27837–27845, https://doi.org/10.1016/j.ijhydene.2020.07.033.
[43] S.P.M. Bane, J.E. Shepherd, E. Kwon, A.C. Day, Statistical analysis of electrostatic spark ignition of lean H2/O2/Ar mixtures, Int. J. Hydrogen Energy 36 (3) (2011) 2344–2350, https://doi.org/10.1016/j.ijhydene.2010.05.082.
[44] A. Kumamoto, H. Iseki, R. Ono, T. Oda, Measurement of minimum ignition energy in hydrogen-oxygen-nitrogen premixed gas by spark discharge, J. Phys.: Conf. Ser. 301 (2011) 012039, https://doi.org/10.1088/1742-6596/301/1/012039.